

This item is the archived peer-reviewed author-version of:

Quantitative STEM normalisation : the importance of the electron flux

Reference:

Martinez Gerardo, Jones L., de Backer Annick, Béch  Armand, Verbeeck Johan, Van Aert Sandra, Nellist P.D..- Quantitative STEM normalisation : the importance of the electron flux
Ultramicroscopy - ISSN 0304-3991 - 159(2015), p. 46-58
DOI: <http://dx.doi.org/doi:10.1016/j.ultramic.2015.07.010>

Quantitative STEM normalisation: The importance of the electron flux

G.T. Martinez^{1*}, L. Jones², A. De Backer¹, A. Béch  ¹, J. Verbeeck¹, S. Van Aert¹, P.D. Nellist²

Abstract

Annular dark-field (ADF) scanning transmission electron microscopy (STEM) has become widely used in quantitative studies based on the opportunity to directly compare experimental and simulated images. This comparison merely requires the experimental data to be normalised and expressed in units of ‘fractional beam-current’. However, inhomogeneities in the response of electron detectors can complicate this normalisation. The quantification procedure becomes both experiment and instrument specific, requiring new simulations for the particular response of each instrument’s detector, and for every camera-length used. This not only impedes the comparison between different instruments and research groups, but can also be computationally very time consuming. Furthermore, not all image simulation methods allow for the inclusion of an inhomogeneous detector response. In this work, we propose an alternative method for normalising experimental data in order to compare these with simulations that consider a homogeneous detector response. To achieve this, we determine the electron flux distribution reaching the detector by means of a camera-length series or a so-called atomic column cross-section averaged convergent beam electron diffraction (XSACBED) pattern. The result is then used to determine the relative weighting of the detector response. Here we show that the results obtained by this new electron flux weighted (EFW) method are comparable to the currently used method, while considerably simplifying the needed simulation libraries. The proposed method also allows one to obtain a metric that describes the quality of the detector response in comparison with the ‘ideal’ detector response.

Keywords

ADF STEM — electron scattering — quantitative STEM — image simulation — EFW method

¹Electron Microscopy for Materials Science (EMAT), University of Antwerp, Gronenborgerlaan 171, 2020 Antwerp, Belgium

²Department of Materials, Oxford University, Parks Road, Oxford OX1 3PH, United Kingdom

*Corresponding author: gerardo.martinez@uantwerpen.be

Contents

1	Introduction	1
2	Experimental considerations	3
2.1	Experimental and image simulation settings	3
2.2	Measurement of the inner and outer angle of the detector	3
2.3	The importance of the electron flux	3
2.4	The electron flux distribution behaviour when averaged over an atomic column	4
2.5	The Scattered Electron Flux Weighted method	6
3	Simulation study	8
4	Experimental analysis of Pt wedge sample	10
5	Conclusions	13
	Acknowledgments	13

A	Appendix A. Measurement of inner and outer collection angles of the ADF detector	14
A.1	Detector inner collection angle	14
A.2	Detector outer collection angle	14
B	Appendix B. List of symbols	15
	References	16

1. Introduction

Scanning transmission electron microscopy (STEM) has become a widespread technique for materials characterisation. When using an annular dark-field detector (ADF STEM), the images obtained from this technique are chemically sensitive, which provide information about the structure and the atomic number Z of the atoms present in the sample [1]. Due to the incoherent nature of the ADF signal, the interpretability of the images is more intuitive than conventional TEM, since there are no contrast reversals. Qualitative matching between experimental and simulated images is common practice when trying to resolve material structures. However, quantitative

methods are required in order to fully extract the structural and chemical information of the material under study, such as the number and types of atoms and their positions in the structure. A route to perform quantitative analysis of ADF STEM images considers the analysis of contrast variation and peak intensity as measures for obtaining the information of interest [2, 3]. The comparison of experimental and simulated images using either Bloch wave method or multislice approach [4, 5, 6, 7] aims to quantify the structure and its composition. For the ADF signal, the inclusion of thermal diffuse scattering (TDS) in the simulations [5, 8, 9] is of critical importance, necessitating the development of absorptive potential [5, 6] or frozen phonon methods [10, 11]. The detector geometry [12], specimen orientation [3], effect of amorphous layer [13], specimen tilt [14], source size broadening [15] and strain effects [12, 16] should also be considered in the simulation algorithm. However, even with the improvement of the simulation methods, direct comparison with experiment was previously not possible due to the lack of an absolute scale.

When normalising the experimental images with respect to the incoming beam, a direct comparison with simulated images is possible [17, 18, 19, 20, 21, 22, 23]. The importance of the detector response is often overlooked leading to discrepancy between experiment and simulation. Recently, more attention has been given to the detection system and it was pointed out that a full characterisation of the ADF detector should be carried out if the highest quality quantitative analysis is to be achieved [17, 18, 24]. This procedure requires the user to scan the STEM probe over the ADF detector to obtain a response map, which has been found to be both inhomogeneous and asymmetric [25, 26]. The detector response at small scattering angles varies significantly from that at higher angles, and therefore, this should be in some way taken into account while performing the image simulations. One method of incorporating this effect is to include a detector sensitivity profile in the image simulations, which rotationally weights the contribution of the scattered electrons with respect to its scattering angle [22, 23]. Including a detector sensitivity profile has allowed significantly improved agreement between experiment and simulated images [21, 23, 27]. Another option proposes the use of an effective scattering angle to compensate the detector's inhomogeneous response [26], which allows the user to adjust the outer collection angle of the detector to match the simulations with the experiment. However, the somewhat arbitrary choice of this parameter may be user subjective and does not then reflect the experimental hardware itself.

Simulation free methods to quantify ADF STEM images were proposed by Van Aert et al. [28, 29]. This approach considers a statistical parameter estimation theory framework, in which the parameters of an empirical incoherent imaging model are estimated by fitting this model to an experimental image. This is done by optimising a criterion of goodness of fit. From the estimated parameters, the so-called scattering cross-sections of the atomic columns are obtained [28, 30],

which have shown to be sensitive to the chemical composition [28] and number of atoms [29, 31, 32], as well as robust to probe parameters [30, 33]. When doing these analyses, the use of atomic scattering cross-sections has shown to be a reliable measure for ADF STEM quantification that allows high accuracy and precision [29, 32, 34]. This statistics based method is not affected by the inhomogeneous detector response, since it extracts the quantitative data in a relative way from the image only. In order to achieve an absolute quantification a combination with image simulations taking into account the detector sensitivity profile is needed. This approach has been shown to allow chemical composition determination of complex structures [27] and to verify number of atoms [29]. Then, by combining statistics based methods with image simulation based methods, a trustful quantification procedure is obtained, since the possible drawbacks of one method are compensated by the other and vice versa. In this work, we discuss the normalisation procedure required for image simulation based methods and we make use of statistics based methods to confirm our results.

Recently, it has been shown that the detector's response can vary drastically between instruments and manufacturers [25], necessitating a careful ADF detector characterisation for each instrument and detector. Incorporating a detector sensitivity profile in simulations for each different kind of detector is challenging due to their specific asymmetric shape and inhomogeneous response. It also requires a library of images to be simulated for every single instrument detector and camera-length for every experiment that is carried out, which is very time consuming when high-throughput quantitative work has to be performed. Simulation software using the absorptive potential approach are limited to include the effect of the detector's response only for the elastic interaction and not the total scattering, thereby leading to errors.

In this work, we propose an alternative method based on measuring the scattered electron flux that reaches the detector in order to normalise the experimental images with respect to the incident beam. Using this method, a measure of the quality of the detector response is calculated which serves as a universal correction factor to the experimental data for this effect. Then, the normalised experimental images can directly be compared with image simulations that assume a detector with a homogeneous (ideal) response. The image libraries depend then on the experimental parameters of inner and outer detector-collection angles at the detection stage. Moreover, these ideal library cross-section values will not change over time, say if a detector or its amplifiers were replaced. While not necessary reaching the same accuracy as simulations that incorporate the detector response variation, the approach proposed here offers more flexibility and simulation time efficiency when performing quantitative ADF STEM. The Electron Flux Weighted method also yields a simple parameter assessing the uniformity of the ADF detector response, ideal for evaluating different detector models for experiment design.

Table 1. Experimental and frozen lattice simulations settings

Acceleration voltage HT	300 kV
Defocus C_1	0 nm
Spherical aberration C_3	-142 nm
Convergence semi-angle α	21 mrad
Spatial incoherence of source FWHM	0.7 Å
HAADF inner collection angle	58 mrad
HAADF outer collection angle	190 mrad
Zone axis	[110]
Supercell periodicity	9 x 9 unit cells
Supercell size	24.97 x 35.31 Å ²
Maximum specimen thickness	8.32 nm
Number of phonon configurations	20
Pixel size of simulated image	0.1394 Å
Pixel size to sample atomic potential	0.0293 Å

2. Experimental considerations

2.1 Experimental and image simulation settings

A platinum wedge sample in [110] zone axis was prepared using the Focused Ion Beam (FIB) lift-out technique in a FEI Helios FIB, using a 30 kV Ga⁺ ion beam for both cutting and thinning, from a selected grain of a polycrystalline Pt bulk sample. Images were acquired in a probe corrected FEI Titan 60-300 kV working at 300 kV with a 21 mrad semi-convergence angle. Convergent Beam Electron Diffraction (CBED) patterns and ADF image simulations of the same material were performed using the frozen lattice multislice approach within the StemSim software [35]. The experimental and simulation settings are described in Table 1.

2.2 Measurement of the inner and outer angle of the detector

In order to perform a quantitative analysis of an ADF image, the instrumental and experimental parameters must be known; these can be measured independently up to a certain degree of accuracy and precision [36]. The accurate measurement of inner and outer collection angle of the ADF detector is of critical importance since the variation of the cross-section value highly depends on it (see Figure 1). To measure the inner angle of the ADF detector, a methodology has been proposed to determine the electron sensitive area of the detector [17], since it may not correspond to the shadow of the detector that is projected on the microscope screen (see Appendix A). Usually, ADF detectors have a dead region surrounding their inner hole that is insensitive to the electron beam. Figure 1 shows the effect on simulated cross-section as a function of thickness for Pt in [110] zone axis that may result if the detector collection angles are mis-measured. For the camera-length used in the experiments presented in this work, the shadow of the ADF detector corresponds to 50 mrad, meanwhile the actual sensitive area of the detector starts at 58 mrad scattering angle. As it can be observed in Figure 1, the choice of the shadow as inner collection angle, that is, a mis-measurement of the inner collection angle by 8 mrad, leads to an overestimation

of the atom cross-section. The same applies for the outer collection angle of the detector. The amount of signal that reaches the detector at high scattering angle can be limited by the post-specimen optics, which depends on the microscope column design. Consequently, this depends on each specific instrument and should be measured as well. A more detailed analysis of the cause of this scattering cut-off will be presented in future work. For our instrument, the measurement of the signal cut-off for the camera-length used was found to be 190 mrad in contrast with the manufacturer's nominal value of 200 mrad. We found that the cut-off is different for each camera length and this should be calibrated accordingly. The variation of cross-section values for different outer angles is also plotted in Figure 1, which shows an overestimation when the manufacturer's value is used instead of the measured one for large sample thickness. It can also be observed that a mis-measurement of the inner collection angle (8 mrad) affects the result more than a similar mis-measurement of the outer collection angle (10 mrad). This cut-off on the signal scattered to high angles also implies that for short camera-lengths, the surface of the detector is not fully illuminated by the electron beam. This fact is of importance since the region close to the hole of the detector shows by far the most inhomogeneous response [25, 26]. A detailed procedure for the inner and outer detector-collection angle measurement is described in Appendix A. Figure 1 (right y-axis) also depicts the behaviour of the image peak intensity for these simulations. Beyond around eight atoms, the peak intensity signal saturates and it becomes harder to distinguish between increasing number of atoms. Since the cross-section measure has shown a monotonic increment with respect to increasing number of atoms [29, 31, 32, 37] and with respect to increasing average atomic column weight [27, 28, 30] and robust to probe parameters [30, 33], we consider this a suitable measure for quantitative ADF analysis and use this through the remainder of this work.

2.3 The importance of the electron flux

The electron flux describes the amount and distribution of scattered electrons that are detected at the diffraction plane. These scattered electrons form the CBED pattern of which a proportion is collected by the ADF detector. Knowing what proportion of the scattered electrons reaches each part of the detector is important because of its inhomogeneous response. Electrons scattered at low angles may experience only one third the detector sensitivity of those electrons scattered at high angles [25]. The signal cut-off at certain high angle also affects the region of the detector that is used during the experiment. Therefore, determining the relative importance of the detector region that is excited by the electron flux allows one to estimate the actual value of the fraction of incident probe that is detected.

The intensity as recorded in the experimental ADF image after black-level subtraction (offset of the amplifier's detector)

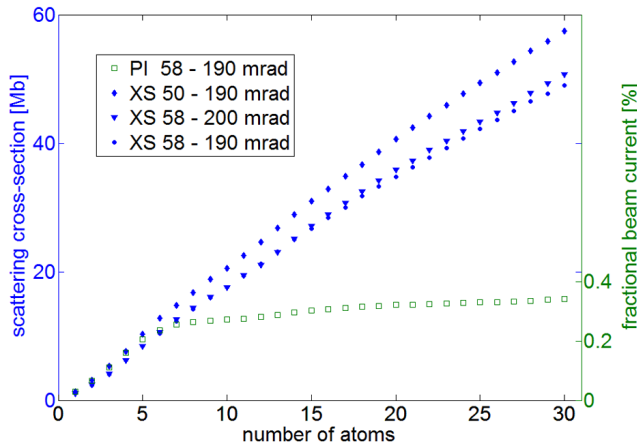


Figure 1. Scattering cross-sections (XS) for Pt in [110] zone axis for different detector angular ranges (1 Megabarn [Mb] = 10^{-22} m^2). Right y-axis shows the behaviour of peak intensities (PI).

can be expressed as:

$$I(\mathbf{r}) = \int F(\mathbf{r}, \mathbf{k}) \cdot D(\mathbf{k}) d^2 \mathbf{k} \quad (1)$$

where $I(\mathbf{r})$ is the image intensity value, $F(\mathbf{r}, \mathbf{k}) = |\psi(\mathbf{r}, \mathbf{k})|^2$ is the electron flux distribution across the diffraction plane, $D(\mathbf{k})$ is the detector's experimental response, $\mathbf{r} = (x, y)^T$ is the real-space position vector and $\mathbf{k} = (k_x, k_y)^T$ is the reciprocal-space vector. It has been shown that this image intensity is in agreement with a simulated reference data calculated with a detector sensitivity profile (hereinafter referred to as the DSP method) [18, 23] when it is normalised with respect to the incident probe, that is:

$$N_{DSP}(\mathbf{r}) = \frac{I(\mathbf{r})}{\bar{D}} = \tilde{N}_{DSP}(\mathbf{r}) \quad (2)$$

with

$$\tilde{N}_{DSP}(\mathbf{r}) = \int \tilde{F}(\mathbf{r}, \mathbf{k}) \cdot \hat{D}_{DSP}(\mathbf{k}) d^2 \mathbf{k} \quad (3)$$

$$\bar{D} = \frac{1}{A_D} \int_{A_D} D(\mathbf{k}) d^2 \mathbf{k} \quad (4)$$

where $N_{DSP}(\mathbf{r})$ is the experimental image intensity normalised with respect to the incident beam, \bar{D} is the normalisation factor usually assumed to be the average detector response when the full electron beam is incident [17, 18] calculated over the whole detector area A_D , $\tilde{N}_{DSP}(\mathbf{r})$ is the simulated image intensity value calculated using a detector sensitivity profile of the experimental detector response, $\hat{D}_{DSP}(\mathbf{k})$, which is a factor defined as $D(\mathbf{k})/\bar{D}$ and $\tilde{F}(\mathbf{r}, \mathbf{k})$ corresponds to the calculated electron flux distribution (simulated CBED pattern). However, it has been discussed previously that the detector response $D(\mathbf{k})$ is inhomogeneous and can vary between detectors [25].

Incorporating its effect in simulated images may be complex. Therefore, the proposed alternative method is based on a homogeneous detector response $\hat{D}_{HDR}(\mathbf{k})$, which satisfies the condition for collection angle β :

$$\hat{D}_{HDR}(\mathbf{k}) = \begin{cases} 1, & \beta_{inner} < |\mathbf{k}| < \beta_{outer} \\ 0, & \text{otherwise.} \end{cases} \quad (5)$$

Now, the simulated intensity values assuming an ideal detector response $\tilde{N}_{HDR}(\mathbf{r})$ become:

$$\tilde{N}_{HDR}(\mathbf{r}) = \int \tilde{F}(\mathbf{r}, \mathbf{k}) \cdot \hat{D}_{HDR}(\mathbf{k}) d^2 \mathbf{k} \quad (6)$$

In order to reliably compare the experimental data with the simplified simulated library, we need to know the relationship between Eq.(1) and Eq.(6). Comparing Eq.(3) and Eq.(6) we have:

$$\tilde{N}_{DSP}(\mathbf{r}) = \xi(\mathbf{r}) \cdot \tilde{N}_{HDR}(\mathbf{r}) \quad (7)$$

where $\xi(\mathbf{r})$ is a proportionality factor defined by:

$$\xi(\mathbf{r}) = \frac{\int \tilde{F}(\mathbf{r}, \mathbf{k}) \cdot \hat{D}_{DSP}(\mathbf{k}) d^2 \mathbf{k}}{\int \tilde{F}(\mathbf{r}, \mathbf{k}) \cdot \hat{D}_{HDR}(\mathbf{k}) d^2 \mathbf{k}} = \int \frac{\tilde{F}(\mathbf{r}, \mathbf{k})}{\tilde{N}_{HDR}(\mathbf{r})} \cdot \hat{D}_{DSP}(\mathbf{k}) d^2 \mathbf{k} \quad (8)$$

Now, combining Eq.(2) and Eq.(7) and making use of the definition of $\hat{D}_{DSP}(\mathbf{k})$ we find that:

$$\tilde{N}_{HDR}(\mathbf{r}) = \frac{I(\mathbf{r})}{\xi(\mathbf{r}) \bar{D}} \quad (9)$$

which states that the simulated intensities using a homogeneous detector response, $\tilde{N}_{HDR}(\mathbf{r})$, can be compared faithfully to the experimental intensities, $I(\mathbf{r})$, when using the appropriate normalisation factor, $\xi(\mathbf{r}) \bar{D}$. Therefore, $\xi(\mathbf{r})$ can be seen as a metric describing the quality of the detector response. Indeed, it relates the experimental detector response to the 'ideal' case. The closer the value of $\xi(\mathbf{r})$ is to 1, the more homogeneous the detector response is. It should be noted that the absolute magnitude of the experimental flux distribution in the detector plane, $F(\mathbf{r}, \mathbf{k})$, will depend on many parameters such as sample thickness, atomic number or local strain. In fact, this is the basis of quantitative ADF, that scattering to the detector increases with increased thickness or increased atomic number. In the next sections we explore the degree to which $\xi(\mathbf{r})$ is robust to these changes and can therefore be used as a universal scaling parameter.

2.4 The electron flux distribution behaviour when averaged over an atomic column

Now, the electron flux distribution $F(\mathbf{r}, \mathbf{k})$, either experimental or calculated, should ideally be available for every probe position, angular collection range of the detector and sample thickness, which is not easily obtained experimentally

or requires high amounts of data storage and computation time. Therefore, it is attractive to find an approximation for this function. Figure 2 a) shows the rotationally averaged simulated CBED pattern for different probe positions, either on or off column, for ADF detector collection angles. We can observe that the behaviour of the signal versus scattering angle highly depends on probe position and it is difficult to model due to highly rapid changes per angle in the profile.

As indicated before, the measure that we use to perform the quantification procedure is the scattering cross-section, which can be obtained either by calculating the volume under a fitted Gaussian function [28] or integrating the pixels over a Voronoi-cell [21, 30] at the atomic column position. This quantity contains the information of the different probe positions that correspond to the scattering cross-section of the atomic column. We can now re-cast $\xi(\mathbf{r})$ as being a correction factor associated with a specific atomic column i , localised at the atomic column position \mathbf{r}_i . Using the following expressions,

$$\sigma_{DSP_i} = \frac{\Theta_i}{\bar{D}} = \tilde{\sigma}_{DSP_i} \quad (10)$$

$$\sigma_{EFW_i} = \frac{\Theta_i}{\xi_i \bar{D}} = \tilde{\sigma}_{HDR_i} \quad (11)$$

where σ_{DSP_i} and σ_{EFW_i} correspond to the normalised experimental cross-section values using the DSP method and the proposed Electron Flux Weighted (EFW) method, Θ_i is the sum of intensity values over a single atomic column multiplied by the pixel size squared obtained from the experimental image after black-level subtraction, $\tilde{\sigma}_{DSP_i}$ is the simulated cross-section using a detector sensitivity profile, $\tilde{\sigma}_{HDR_i}$ is the simulated cross-section obtained assuming a homogeneous detector response, $\xi_i = \xi(\mathbf{r}_i)$ is the scaling factor for atomic column i and \bar{D} have been defined previously. From Eq.(10) and Eq.(11), it is straightforward that:

$$\tilde{\sigma}_{HDR_i} = \frac{1}{\xi_i} \cdot \tilde{\sigma}_{DSP_i} \quad (12)$$

which allows us to compare both methods by using image simulations. The question now arises of the degree to which ξ_i is robust to changes in thickness and composition and can be used as a universal parameter over the whole image.

We can average the CBED patterns of each probe position that form the scattering cross-section of the atomic column to obtain a cross-section averaged convergent beam electron diffraction pattern (XSACBED). This procedure is similar as obtaining a Position Averaged Convergent Beam Electron Diffraction pattern (PACBED) [38, 39], but instead of averaging the probe positions of the whole unit cell, only the probe positions that form the scattering cross-section of the column are taken into account. In this way, we can express the electron flux distribution of the atomic column cross-section as:

$$F_{XS}(\mathbf{r}_i, \mathbf{k}) = \int_{\zeta_i} F(\mathbf{r}, \mathbf{k}) d^2 \mathbf{r} \quad (13)$$

where \mathbf{r}_i corresponds to the position vector of the i th atomic column, ζ_i is the cross-section area of the i th atomic column and \mathbf{r} and \mathbf{k} have been defined previously. This function is the sum of the electron flux over the corresponding image pixels used to calculate the scattering cross-section. It can be seen as the function describing the total electron flux distribution originated from an atomic column i . In this manner, Eq.(8) can be rewritten as:

$$\begin{aligned} \xi_i = \xi(\mathbf{r}_i) &= \frac{\int \tilde{F}_{XS}(\mathbf{r}_i, \mathbf{k}) \cdot \hat{D}_{DSP}(\mathbf{k}) d^2 \mathbf{k}}{\int \tilde{F}_{XS}(\mathbf{r}_i, \mathbf{k}) \cdot \hat{D}_{HDR}(\mathbf{k}) d^2 \mathbf{k}} \\ &= \int \frac{\tilde{F}_{XS}(\mathbf{r}_i, \mathbf{k})}{\tilde{N}_{HDR}(\mathbf{r}_i)} \cdot \hat{D}_{DSP}(\mathbf{k}) d^2 \mathbf{k} \end{aligned} \quad (14)$$

where $\tilde{F}_{XS}(\mathbf{r}_i, \mathbf{k})$ corresponds to the calculated XSACBED pattern of the atomic column at position \mathbf{r}_i and $\tilde{N}_{HDR}(\mathbf{r}_i)$ is the simulated cross-section value of the i th atomic column at position \mathbf{r}_i assuming an homogeneous detector response. $\hat{D}_{DSP}(\mathbf{k})$ and $\hat{D}_{HDR}(\mathbf{k})$ have been defined in the previous section.

Now, the scaling factor $\xi_i = \xi(\mathbf{r}_i)$ is calculated as a function of the scattering cross-section of the atomic column at a certain position \mathbf{r}_i . In order to explore the degree to which ξ_i can be treated as a universal parameter over an image, we write the XSACBED flux distribution with the following functional form:

$$F_{XS}(\mathbf{r}_i, \mathbf{k}) \approx A_i G_i(\rho) \quad (15)$$

in which A_i corresponds to a scaling factor and $G_i(\rho)$ describes the electron flux behaviour as a function of scattering angle ρ for the i th atomic column. We have found that for high scattering angles (e.g. $\rho > 2\alpha$, with α being the convergence semi-angle), this function can be approximated as follows:

$$F_{XS}(\mathbf{r}_i, \mathbf{k}) \approx A_i G_i(\rho) = A_i \rho^{-b_i} \quad (16)$$

with A_i and b_i fitting variables which can be obtained by various methods. If we substitute Eq.(16) in Eq.(14) and assuming rotational symmetry of the electron flux, we find that:

$$\xi_i = \frac{2\pi A_i \int \rho^{1-b_i} \cdot \hat{D}_{DSP}(\rho) d\rho}{2\pi A_i \int \rho^{1-b_i} \cdot \hat{D}_{HDR}(\rho) d\rho} \quad (17)$$

from where we can understand that the detector quality factor ξ_i only depends on the behaviour of electron flux interacting with the detector's response for the scattering collection angle range, and any change in the overall scaling, A_i , cancels in Eq.(17). To validate the use of a universal correction factor over the whole ADF field of view, we require that the exponent b of the power-law of every atomic column present in the image should remain as near constant as possible and that changes in the thickness and composition predominantly affect the scaling factor, A_i . Indeed, other approximations may be used in Eq.(16). The universality of ξ will still apply as

long as changes in thickness and composition provide predominantly a scaling effect rather than changes to the functional form.

The approximation described in the previous paragraph is tested in Figure 2 b). The gradient of the plots on this logarithmic-scale, and hence the flux distribution profiles tend to behave similarly for increasing number of atoms. The power-law function is fitted to these profiles, from which the normalisation factor $\xi\bar{D}$ for each thickness is obtained. Figure 2 c) shows the obtained b exponent values of the power-law fit for these profiles as a function of the number of atoms present in the atomic column. It can be observed that the exponent b tends to stabilise its value with increasing number of atoms. The validity of using the power-law function as a description of the scattering electron flux and for approximating $\xi\bar{D}$ by a constant for different thickness and composition is discussed in the simulation study presented later in this work.

2.5 The Scattered Electron Flux Weighted method

In this section the Electron Flux Weighted (EFW) method is introduced. For this method, the electron flux reaching the detector plane needs to be determined. Figure 3 shows two different ways to determine the scattered electron flux. The use of an experimental or simulated XSACBED allows one to fit the power-law function between the inner and outer angles determined in section 2.2. Figures 3 a) and c) show a simulated XSACBED pattern from a 30 atoms thick Pt [110] sample and its rotationally averaged profile, to which a power-law function is fitted. Another option is to perform a camera-length (CL) series [40], from which the electron scattering profile can also be measured. In order to obtain the scattering electron flux from a camera-length series, one should record or simulate a series of images from the same sample area at the different camera-lengths available at the microscope. Then, the image intensity per detector area from a chosen region should be integrated and plotted with respect to scattering angle, Figure 3 b). The variation of intensity with respect to scattering angle can be computed by taking the difference in integrated signal of consecutive camera-lengths, which leads to the scattering electron flux, also plotted in Figure 3 c). One can see that both techniques lead to similar results.

After determining the behaviour of the scattering electron flux, we need to obtain the normalisation value $\xi\bar{D}$ using electron flux weighting. Figure 4 shows the steps to be followed for this. First, an ADF detector scan is needed (Figure 4 a), which corresponds to the experimental detector function $D(\mathbf{k})$. The inner and outer collection angles should be measured and the active detector area is identified in this detector map, (Figure 4 b), resulting in the homogeneous detector response $\hat{D}_{HDR}(\mathbf{k})$. Using the knowledge of the flux cut-off angle, determined from an experimental flux-map (see Appendix A.2), this can be shaded in two parts; the white region shows the illuminated area, while the grey area shows the active but not illuminated area. The illuminated region is used

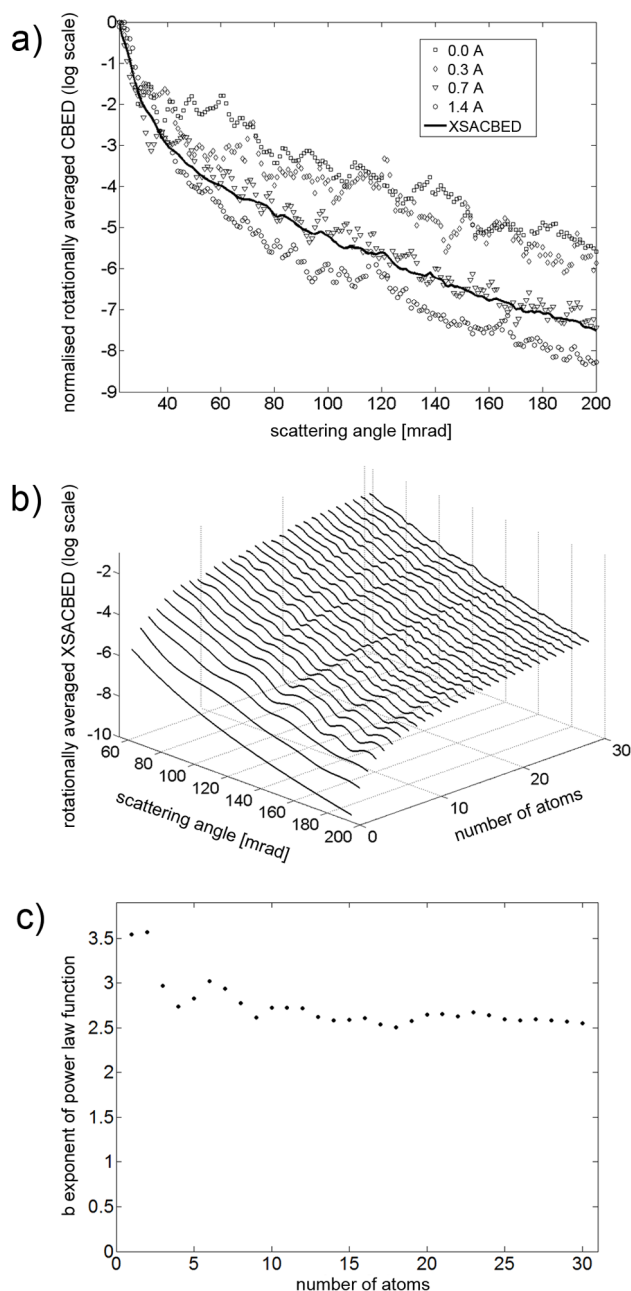


Figure 2. a) Scattered points show rotationally averaged CBED pattern (22-200 mrad) for different probe positions: on column, 0.3Å, 0.7Å and 1.4Å away from the atomic column of a 30 atoms thick Pt [110] sample. Solid line represents the rotationally averaged XSACBED. b) Rotationally averaged XSACBED (58-190 mrad) averaged over atomic column area for increasing number of atoms (logarithmic-scale). c) Fitted b exponent of power-law function as a function of number of atoms present in the atomic column.

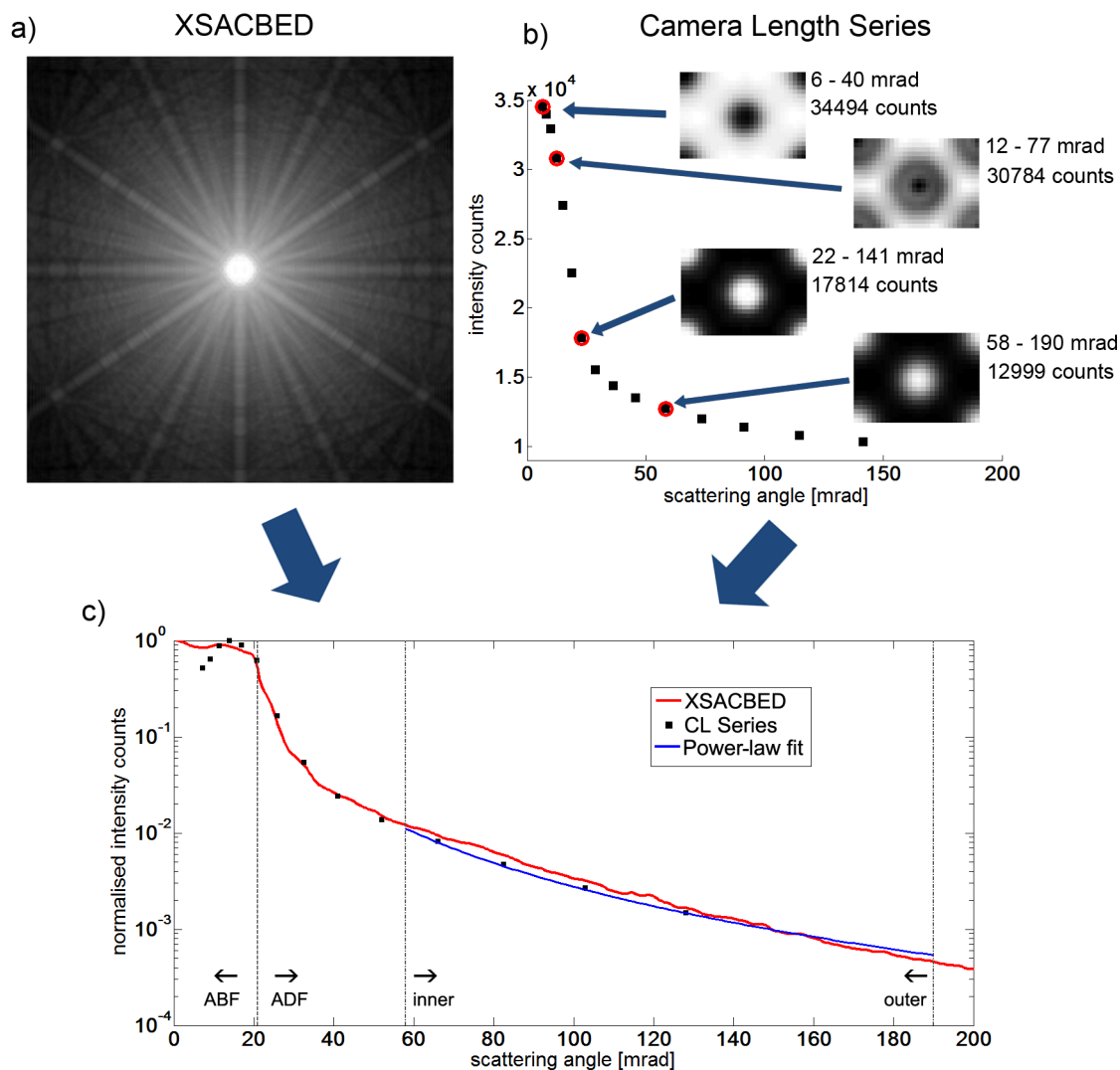


Figure 3. Methods to model the scattered electron flux. a) Simulated XSACBED of Pt in [110]. b) Plot of intensity counts from simulated images versus inner collection angle. Figure insets show simulated example images of a Pt unit cell for different camera-lengths. The variation in contrast and amount of signal is explained by the different detector regimes, such as ABF, LAADF or HAADF. c) Rotationally averaged XSACBED (red line), electron flux obtained from CL series (black dots) and power-law fit (blue line) from inner and outer detector angles used in experiment. Note that the rotationally averaged XSACBED signal and scattered electron flux data points were normalised in order to be compared.

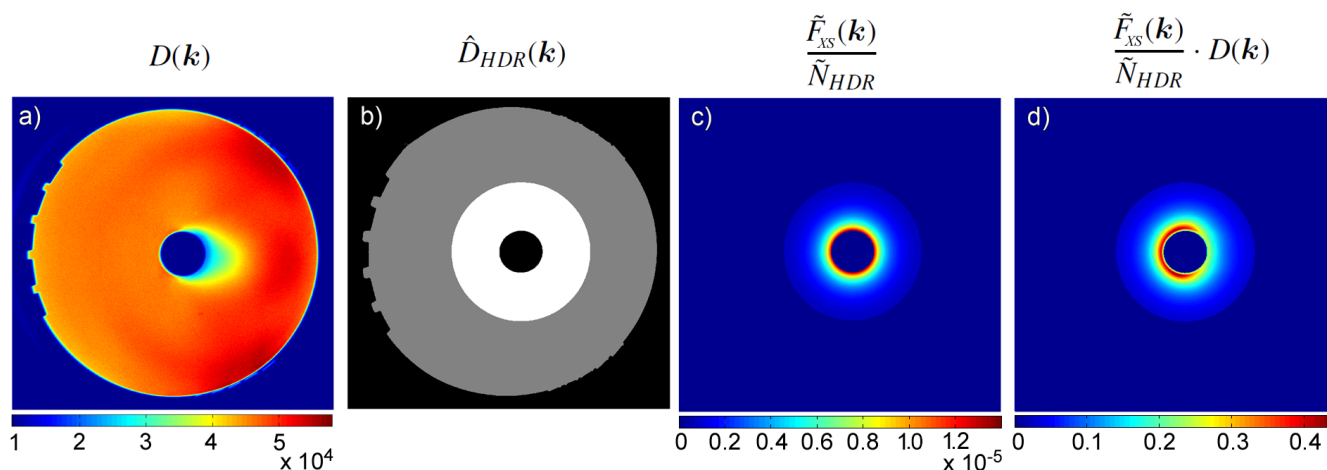


Figure 4. Scattered electron flux weighted method. a) Map of ADF detector. b) ADF detector illuminated region (white region). Grey region corresponds to the area of detector that is active but not illuminated for this camera-length. c) Modelled scattered electron flux using power-law function obtained from XSACBED or CL series reaching the illuminated area of the detector. d) Scattered electron flux weighted by the ADF detector inhomogeneous response. For this example, the weighting factor $\xi = 0.86$.

to calculate the weighted average sensitivity. Note, how for this camera-length, the whole area of the detector spans up to ≈ 400 mrad, however, only a fraction of this detector area (22.5%) is actually illuminated by the electron flux and used to record a signal. Next, we calculate the rotationally averaged electron flux within the illuminated region of the detector. For this, we use the power-law function determined previously, which is calculated within the illuminated area of the detector and then divided by the total intensity of the electron flux reaching that portion of the detector. This step is shown in Figure 4 c) and corresponds to computing $\tilde{F}_{XS}(\mathbf{k})/\tilde{N}_{HDR}$. Finally, the normalised electron flux image is multiplied pixelwise with the ADF detector image to obtain the scattered electron flux weighted by the ADF detector inhomogeneous response, giving Figure 4 d). Taking into consideration all three factors (the flux profile, the flux cut-off, and the detector's inhomogeneous sensitivity), we arrive at an accurate measure of $\xi\bar{D}$. This integration corresponds to computing Eq.(14) multiplied by \bar{D} . Now we can normalise the experimental images and compare them with simulated ones using a homogeneous detector response. This approach also allows the operator to intuitively visualise the relative importance of each part of the ADF detector. The effect of the inhomogeneous detector response is clearly visible at low scattering angles.

3. Simulation study

To evaluate the procedure of normalising experimental images by the scattered electron flux weighted (EFW) method, we compare its performance against the current method which uses a detector sensitivity profile (DSP method). Figure 5 a) shows the scattering cross-sections obtained from simulations when either a homogeneous detector response, $\hat{D}_{HDR}(\mathbf{k})$, or a detector sensitivity profile, $\hat{D}_{DSP}(\mathbf{k})$ are considered. Using

Eq.(12), the scattering cross-sections from image simulations using a detector sensitivity profile are converted to the scattering cross-sections simulated for a homogeneous detector response. The agreement between the cross-section analyses returned by the two methods demonstrates their equivalence up to a certain thickness (vertical dotted line). Since the scattered electron flux depends on atomic number and sample thickness, we can extend the previous analysis to test up to what extent the power-law assumption holds. For the case of sample thickness, we calculated the value of ξ_i for sample thicknesses ranging from 1 atom to 30 atoms thick. Then, using the values of ξ_i for 1 atom, 30 atoms and the mean value from 1 up to 30 atoms, $\bar{\xi}_i$, we converted the scattering cross-section values obtained by DSP simulations using Eq.(12) for the different ξ_i values. Figure 5 b) shows the computed atom counting error when comparing the converted cross-sections to HDR simulations. An atom counting error higher than 0.5 indicates that there will be 1 atom mismatch when comparing the cross-section values. If the weighting factor ξ_i assuming the scattering electron flux of 1 atom is used, then there is an overestimation of the cross-section values for thicknesses higher than ≈ 10 atoms. When using the weighting factor ξ_i calculated for 30 atoms thickness or the mean value $\bar{\xi}_i$, the atom counting error remains lower than 0.5 up to a sample thickness of 20 atoms. For higher thickness, it systematically increases. This means that, for example, when measuring the electron flux using the camera-length series method, we can choose an area of the image with several unit cells and varying thickness, and the normalisation factor that we get is still acceptable for normalising the whole field of view for reasonably thin specimens. For thicker specimens, the power-law behaviour deviates and this adds a 1 atom error to other sources of error that have been studied elsewhere [41]. In contrast, if the inhomogeneity of the detector's response would

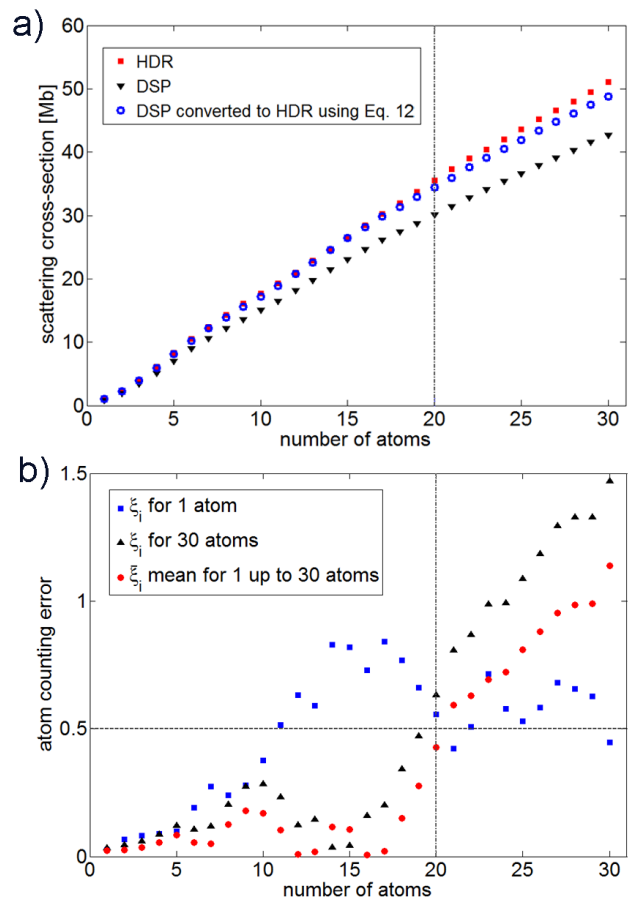


Figure 5. a) Scattering cross-sections obtained from image simulations assuming either $\hat{D}_{HDR}(\mathbf{k})$ or $\hat{D}_{DSP}(\mathbf{k})$ detector responses. Using Eq.(12), the cross-sections obtained from image simulations using a detector sensitivity profile are converted to the cross-sections for a homogeneous detector response. Vertical dotted line indicates the thickness up to which the power-law holds and the two methods are equivalent. b) Atom counting error when converting the scattering cross-section values using Eq.(12) for ξ_i weighting factor calculated for 1 atom (blue squares), 30 atoms (black triangles) and the mean value $\bar{\xi}_i$ from 1 up to 30 atoms (red circles). Above horizontal dotted line indicates the possibility to mismatch over 1 atom. Vertical dotted line indicates the thickness up to which both methods are equivalent.

not be taken into account in the simulations, there would be an error of miscounting 1 atom already by a sample thickness of 5 atoms (see Figure 5 a), which increases systematically to lead an error to miscount by 4 atoms for a sample thickness of 20 atoms, for example.

The weighting factor ξ_i is a measure of how the detector inhomogeneous response affects the scattered flux of the i th atomic column in the sample. It is a performance metric of the quality of the ADF detector's response. For example, the value of ξ_i for 1 atom corresponds to 0.82, whereas for 30 atoms is 0.87 and for the mean value $\bar{\xi}_i$ is 0.86. The closer the ξ_i value is to one, the more similar the response is to that of an 'ideal' detector. Then, the scattered electron flux for 1 atom is affected more by the inhomogeneous response of the detector. This can be understood by observing Figure 2 b). The scattered flux for 1 atom decays rapidly for high scattering angles, thus the main contribution to the intensity is detected at low scattering angles, where the inhomogeneous detector response is more prominent. For the 30 atoms case, the scattered electron flux reaches higher scattering angles, where the detector's response is more homogeneous and the overall contribution is less affected by the inhomogeneity at low scattering angles.

To test the validity of using a constant exponent in the power-law approximation for a composition analysis, we studied two bimetallic examples. We simulated bulk crystals of Cu, Pd, Pt, $\text{Cu}_{0.5}\text{Pt}_{0.5}$ and $\text{Pd}_{0.5}\text{Pt}_{0.5}$ and analysed the ξ_i factors for each species for a 30 atoms thick sample. Figure 6 a) shows the calculated ξ_i factors as a function of averaged atomic weight of the column. Blue circles correspond to the calculated ξ_i value when fitting the power-law function to the rotationally averaged simulated XSACBED for each material. The ξ_i factors behave very similar for the different atomic species and they show a small increment with increasing atomic weight. This is expected, since the scattering power of heavier atomic columns leads to more signal at higher scattering angles, where the response of the detector is more homogeneous. Next, we tested the possibility of using an averaged exponent of single element columns to model the scattering electron flux of the mixed species material. For example, the fitted exponent of the pure Cu and the pure Pt crystals were averaged in a 50% – 50% relation. This averaged exponent was used to model the scattering electron flux of the $\text{Cu}_{0.5}\text{Pt}_{0.5}$ column. Inverted black triangles in Figure 6 a) indicate the results for the two bimetallic examples considered in this work. The similarity between the ξ_i factors when fitting the power-law function to the mixed species simulation or when averaging the exponents of the pure columns is within 0.1%. Figure 6 b) shows the simulated scattering cross-sections for these single and mixed species crystals when using either HDR or DSP methods. Using Eq.(12), the cross-sections obtained from DSP method were converted to HDR method using the calculated ξ_i factors for each type of material. For the mixed columns, the ξ_i factors obtained from averaging the exponents of the pure columns were also used

for comparison. The ratio in percentage of cross-section value when using the true exponent obtained from the simulation considering the mixed composition of the atomic column and when using the averaged exponent of pure atomic columns is $\approx 0.1\%$. These results indicate the possibility to normalise the experimental image with a ξ_i factor obtained from averaged exponents of the pure columns present in the sample when analysing columns with mixed composition. Then, a robust behaviour of the power-law approximation with respect to composition variation is found. From the previous discussion we can conclude that the power-law behaviour is robust to thickness and composition variations in the atomic column. This implies that the electron flux can be averaged over the whole field of view. Then, the dependence of it with respect to atomic column position r_i is not necessary. Therefore, the use of a universal scaling factor ξ to normalise the whole field of view is justified, as introduced in section 2.4. A more detailed analysis of the validity of power-law behaviour with respect to other microscope variables such as accelerating voltage, convergence angle, chromatic aberration, different collection angle regimes or more complex atomic species arrangements in the column are subjects of future work.

An overview of the similarities and differences between the two methods is depicted in Figure 7. This schematic summarises how the detector is considered for the DSP and EFW methods. Using the DSP method, the experimental images are normalised by a factor which is calculated assuming that the detector has an equal response over all its active area and consequently a detector sensitivity profile must be included when simulating reference images. This scaling factor profile is determined by rotationally averaging the inhomogeneous response of the detector. For the case of the EFW method, the detector used for normalisation is the actual detector response that the electron excites and therefore it shows the relative importance of the detector response due to its inhomogeneity. Then, the detector profile used in simulations for this method only requires a constant response of unity between the inner and outer angle of the detector. One could use the DSP detector normalisation and include a detector sensitivity profile in the simulation for the quantification of the experimental image, or one could normalise it using the electron flux weighted method and compare it to simulations with a homogeneous detector response. However, both normalisation method work-flows should not be mixed.

4. Experimental analysis of Pt wedge sample

In section 3 we demonstrated the validity of the EFW method using simulated data (Figure 5), but the same test can be repeated experimentally, here using ADF STEM images of a Pt wedge sample in [110] zone axis. An experimental camera-length series from the sample was performed in order to measure the scattered electron flux. The image series were brought into register [42] to obtain the total number of counts per image area, from which the electron flux profile was estimated,

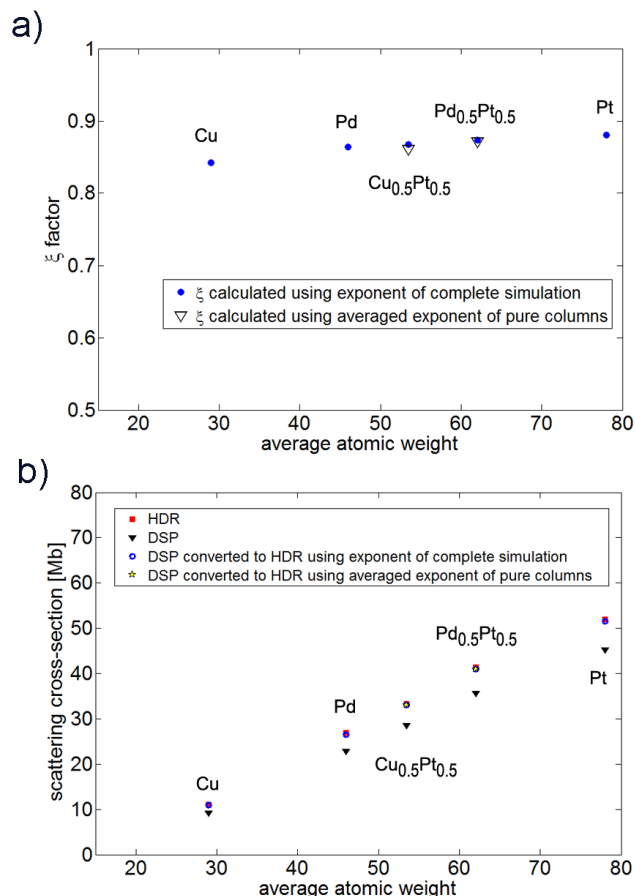


Figure 6. a) ξ factor as a function of averaged atomic weight. Blue dots correspond to the ξ factors obtained from fitting the power-law function to rotationally averaged XSACBED patterns of simulations containing single element columns (Cu, Pd, Pt) and mixed bimetallic ($\text{Cu}_{0.5}\text{Pt}_{0.5}$, $\text{Pd}_{0.5}\text{Pt}_{0.5}$) columns. Inverted black triangles correspond to the obtained ξ factors for mixed columns when averaging the exponent of the power-law function of pure columns. b) Simulated scattering cross-sections as a function of averaged atomic weight for HDR (red squares) and DSP (black triangles) methods. Using Eq.(12), the cross-sections were converted from DSP to HDR methods using the ξ factors obtained from the power-law functions fitted to the complete simulations (blue circles) and from the averaged exponent obtained from single species columns (yellow stars).

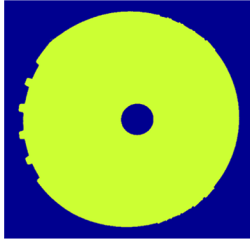
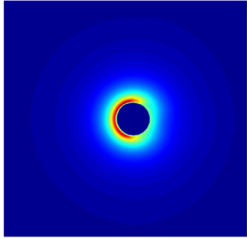
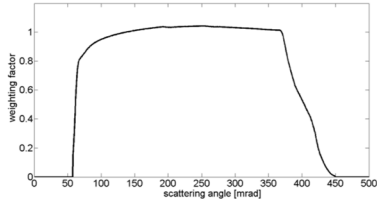
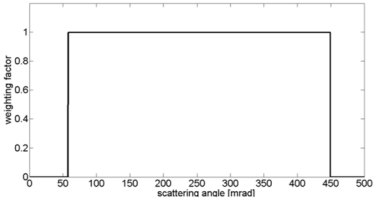
	DSP	EFW
Detector used for experimental normalisation		
Normalisation factor	$\bar{D} = \frac{1}{A_D} \int_{A_D} D(\mathbf{k}) d^2 \mathbf{k}$	$\xi \bar{D} = \int \frac{\tilde{F}(\mathbf{k})}{\tilde{N}_{HDR}} \cdot D(\mathbf{k}) d^2 \mathbf{k}$
Detector profile used for image simulation	 $\hat{D}_{DSP} = \frac{D(\mathbf{k})}{\bar{D}}$	 $\hat{D}_{HDR}(\mathbf{k}) = \begin{cases} 1, & \beta_{inner} < \mathbf{k} < \beta_{outer} \\ 0, & \text{otherwise.} \end{cases}$
Cross-section normalisation relationship	$\sigma_{DSP} = \frac{\Theta}{\bar{D}} = \tilde{\sigma}_{DSP}$	$\sigma_{EFW} = \frac{\Theta}{\xi \bar{D}} = \tilde{\sigma}_{HDR}$
Method relationship	$\sigma_{EFW} = \frac{1}{\xi} \cdot \sigma_{DSP}$ $\tilde{\sigma}_{HDR} = \frac{1}{\xi} \cdot \tilde{\sigma}_{DSP}$	

Figure 7. Overview of differences and equivalences for DSP and EFW methods for the general case. The cut-off of the signal at high scattering angles should be included depending on the camera-length, as it is shown in Figure 4 for the 91 mm camera-length.

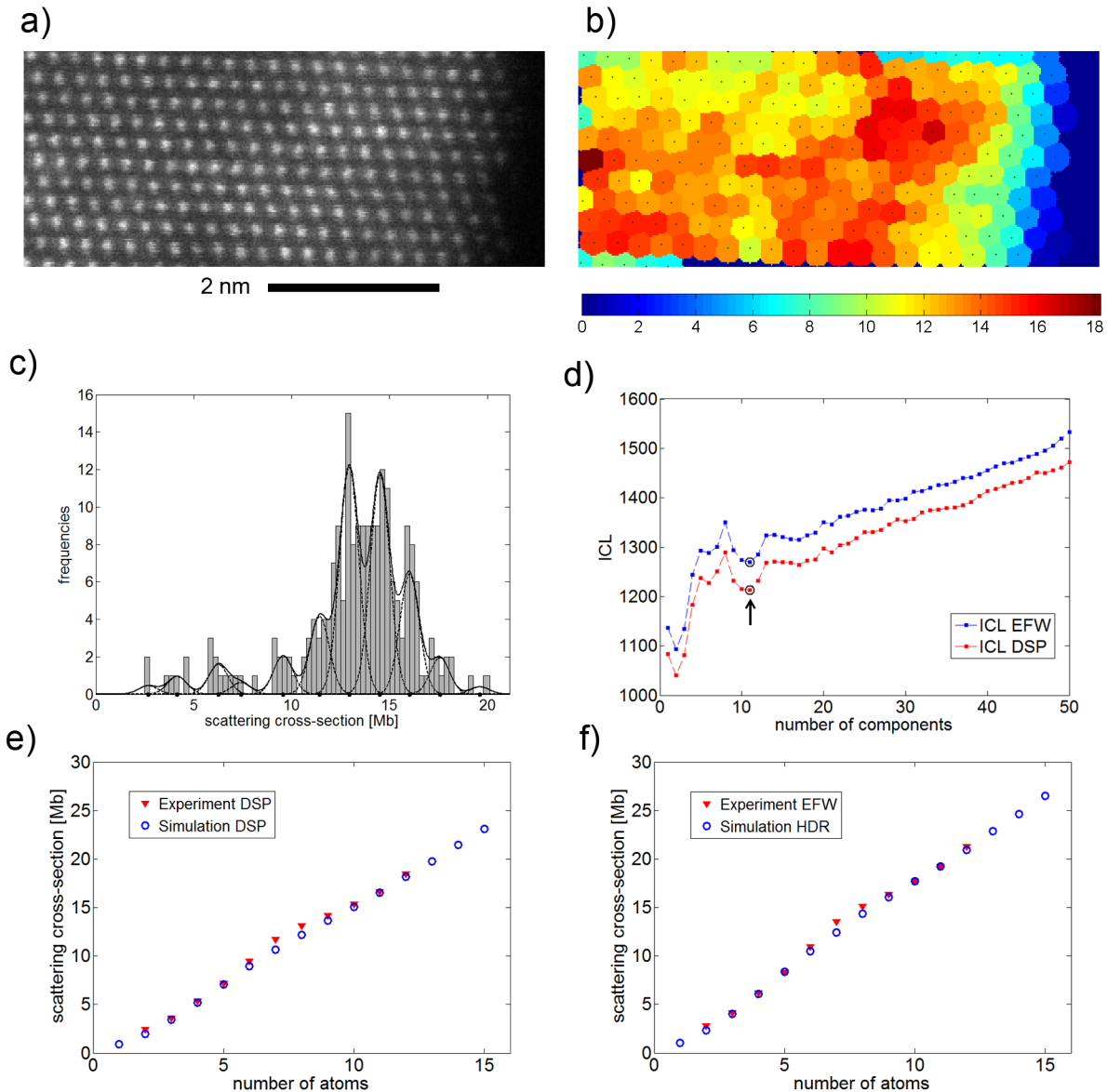


Figure 8. Experimental quantification of Pt wedge sample. a) Experimental image used for quantification. b) Cross-sections map obtained from Absolute Integrator Software [43]. c) Experimental scattering cross-sections histogram and estimated Gaussian mixture model [29]. d) Order selection criteria for both methods. Arrow shows the minimum value that defines the number of components in the Gaussian mixture model. e) Comparison of cross-sections obtained from experimental image normalised using DSP method and simulations considering a detector sensitivity profile. f) Comparison of cross-sections obtained from experimental image normalised using EFW method and simulations assuming a homogeneous detector response.

as described in section 2.3. The scattering cross-sections were analysed using the Absolute Integrator Software [43] which allows the user to choose either the DSP or EFW type of normalisation methods. The computed scattering cross-sections were used as an input for the statistics based atom counting method described by Van Aert et al. [29], which is independent of image simulations and experimental normalisation procedure. This method allows one to identify the mean scattering cross-section value of an atomic column that would correspond to a specific number of atoms by inferring its probability distribution from the experimental scattering cross-sections. These values can also be compared with a library of simulated scattering cross-sections for confirmation [29]. Figure 8 shows the results for this image quantification when using the DSP and the EFW methods. Figure 8 a) shows the experimental section that was analysed. Figure 8 b) displays the outcome from the Absolute Integrator Software, where the scattering cross-sections were computed. Then, Figure 8 c) shows a histogram of cross-sections and the Gaussian mixture model that is fitted to the cross-section values. By fitting an optimised number of Gaussian functions to the experimental scattering cross-section values, the number of atoms corresponding to a specific cross-section can be determined. The procedure to optimise the number of Gaussian functions is based on an order selection criterion, which is shown in Figure 8 d) for both methods. From this analysis, 11 components are selected. Indeed, the number of statistically significant Gaussian functions usually corresponds to a local rather than to a global minimum of the evaluated order selection criterion [32]. The estimated Gaussian mixture model is shown in Figure 8 c). Based on this estimated probability distribution, the number of atoms in a particular projected column can be identified by assigning each scattering cross-section to the component of the mixture model with the largest probability to generate this scattering cross-section. Then, the mean experimental scattering cross-sections, corresponding to the locations of these 11 components, using the DSP and EFW methods are compared to their corresponding simulated cross-sections in Figure 8 e) and f). The match of cross-section values between experiment and simulations agrees in both methods and showed consistent atom counting results. Therefore, the quantification of experimental images using both normalisation methods is demonstrated to be equivalent and it is confirmed by the simulation independent statistics based atom counting method.

5. Conclusions

Quantitative analysis of ADF STEM images is possible when the experimental image is normalised with respect to the incident beam, allowing a direct comparison between experimental data and simulated images. The use of a detector sensitivity profile (DSP method) while carrying out the image simulations has improved the comparison with the experiment. This approach requires detailed inclusion of the detector's response for the calculation, which makes the image simulation

libraries specific for a detector type or experiment. When a high-throughput image quantification is required, the previous approach can be very time consuming since the need of simulating specific libraries for each experiment and detector. In this work, we have presented an alternative method to normalise the experimental image by electron flux weighting, which allows one to compare the experimental images with simulated ones that consider a homogeneous detector response. Evaluating the two analysis options, we have found that the accuracy of the proposed EFW method is equivalent to the DSP method up to a certain sample thickness (20 atoms for Pt structure). It is also possible to use the average exponent of the power-law function of single species atomic columns to normalise images with atomic columns with mixed composition. This allows the possibility to have a simulation library database that is reusable and adaptable to different detector responses. Using the proposed work-flow of the EFW method, the simulation image resources, such as computing capabilities, simulation algorithms or softwares, can be optimised, since it is not necessary to include the detector's response in the computation. Both methods require the accurate measurement of the inner and outer angle of the ADF detector and their two work-flows should not be mixed. As in other literature, we also find the use of scattering cross-sections as a preferred measure for quantitative ADF analysis. The cross-sections of normalised experimental images using the DSP and EFW methods showed an excellent agreement with their corresponding simulations. In addition, the simulation independent statistics based atom counting method confirmed the experimental normalisation procedures by showing consistent atom counting results for both approaches. Using the EFW method, a performance metric for the quality of the ADF detector's response (ξ) is also computed, since it relates the detector experimental response to an 'ideal' detector's response. The closer the value of ξ is to 1, the more homogeneous the detector response is.

Acknowledgments

The authors acknowledge financial support from the Research Foundation Flanders (FWO, Belgium) through project fundings G.0368.15, G.0369.15, G.0374.13, G.0044.13 and a Ph.D. research grant to A.D.B.

A.B. and J.V. were supported by funding from the European Research Council under the 7th Framework Program (FP7), ERC grant N°246791-COUNTATOMS and ERC Starting Grant N°278510-VORTEX. The research leading to these results has received funding from the European Union 7th Framework Programme [FP7/2007-2013] under grant agreement N°312483 (ESTEEM2).

The authors are grateful to D. Batuk for assisting in sample preparation, to P. Tiemeijer for useful discussion about the microscope column design and to A. Rosenauer for providing access to the StemSim software.

Appendix A. Measurement of inner and outer collection angles of the ADF detector

A.1 Detector inner collection angle

The measurement of the inner collection angle of the HAADF detector was carried out by two different procedures. The purpose of these procedures is to define the size of the non-electron sensitive layer around the central hole of the detector, which shadow can be visualised on the phosphorous screen/CCD. By measuring angle calibrated images of these shadow at the different camera-lengths and knowing the width of this layer, the inner collection angle of the detector can be determined.

The first procedure [17] consists on shifting the Ronchigram in Diffraction Mode (without sample) until a signal is detected in the ADF detector. Then, images of the Ronchigram with and without the ADF detector inserted are recorded from several Ronchigram positions. Afterwards, all the obtained images are added in order to identify the non-electron sensitive layer. The brighter areas of the Ronchigram will show the shadow circle of the detector while the dimmer area will show where the electron-sensitive layer of the detector starts. From this image, the shape of this layer can be estimated in order to properly centre the Ronchigram. Figure A1 a) shows the final image obtained after adding the different images at several Ronchigram positions for a camera-length of 29 mm. The centre circle of the image is also used for image calibration in angle space since its radius corresponds to the probe convergence semi angle. From this image, it is distinguishable that the non-electron sensitive layer is not radially symmetric since it is broader at the left bottom of the image in comparison with the right upper part.

The second procedure is available for two overlapping detectors, the HAADF and DF4 detectors in the present case. A detector map is obtained in Image Mode with the HAADF and DF4 detectors inserted simultaneously. Two separate images will be obtained with the probe positioned response of each of the detectors. Next, the two images are added and a dark region at the HAADF detector hole will be visible. This region corresponds to the non-electron sensitive layer, since it is the part of the HAADF detector that is stopping the beam to reach the DF4 detector. Figure A1 b) shows the added images, with a close up view of this detector region. As expected, the non-sensitive layer of the HAADF detector shows the same geometry as obtained with the previous method. The ratio sensitive/non-sensitive angle is approximately 1.15 for this case. By measuring the shadow of the detector and multiplying by 1.15, the inner collection angle for each camera-length is obtained.

A.2 Detector outer collection angle

The outer detector angle of the HAADF detector could be considered to be 6.2 times the inner detector angle from computing the ratio between the outer rim of the detector and the inner hole, as appreciated in Figure A1 b). The detector is not

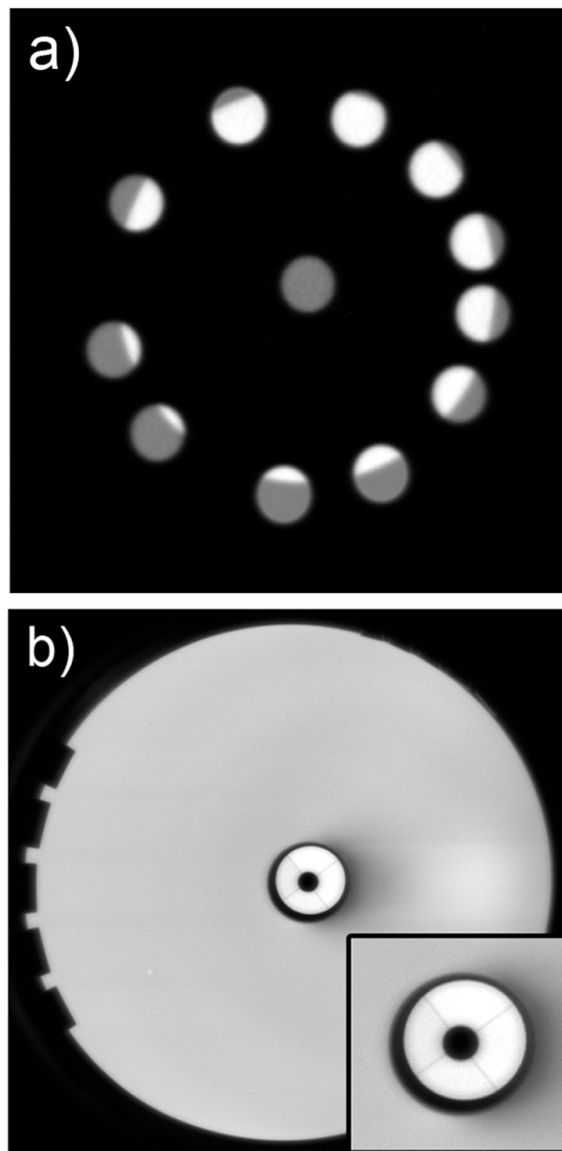


Figure A1. Procedures to measure the inner collection angle. a) Sum of images obtained by shifting the Ronchigram to several positions and acquiring with and without the HAADF detector inserted. b) Sum of images of HAADF and DF4 detectors while scanning the probe at the same time. Inset shows a close up view of the non-sensitive layer of the HAADF detector.

completely roundly symmetric [25], so this value is approximate. However, this relation only holds for camera-lengths where the complete detector is illuminated by the electron scattering flux. Due to microscope design in the projector system, the excitation of the projector lenses and the differential apertures can limit the scattering angle that reaches the detector. This is of importance, since for short camera-lengths, some area of the detector will not be excited by the scattered electron beam. In order to measure the outer cut-off angle, an image of the Ronchigram with a highly scattering sample is recorded with the CCD camera. This image shows a sudden loss of signal at this cut-off angle. Figure A2 a) shows a section of the Ronchigram on the CCD where the cut-off of the signal can be appreciated. Inner white dotted circle represents the BF disk and the outer grey dotted line serves as a guide to the eye to appreciate the loss of signal. In Figure A2 b), a rotationally average from the Ronchigram centre was performed in order to determine the cut-off angle. For the camera length shown in this image, the cut-off of the signal was found to be ≈ 160 mrad. Depending on the settings of the projector lenses for each camera-length, this cut-off value can change, which needs to be characterised for each instrument or calibrated to a fixed cut-off.

Appendix B. List of symbols

A list of symbols for the equations used in this work are presented next.

A_D	ADF detector area
A, b	fitting variables of power-law function
$D(\mathbf{k})$	detector's experimental response
\bar{D}	average detector response
$\hat{D}_{DSP}(\mathbf{k})$	detector response function using a detector sensitivity profile
$\hat{D}_{HDR}(\mathbf{k})$	detector response function from 'ideal' detector
$F(\mathbf{r}, \mathbf{k})$	experimental electron flux distribution across the diffraction plane (CBED pattern)
$F_{XS}(\mathbf{r}_i, \mathbf{k})$	experimental electron flux distribution averaged over the atomic column scattering cross-section (XSACBED pattern)
$\tilde{F}(\mathbf{r}, \mathbf{k})$	simulated electron flux distribution across the diffraction plane (CBED pattern)
$\tilde{F}_{XS}(\mathbf{r}_i, \mathbf{k})$	simulated electron flux distribution averaged over the atomic column scattering cross-section (XSACBED pattern)
$G(\rho)$	electron flux behaviour as a function of scattering angle
$I(\mathbf{r})$	experimental image intensity
\mathbf{k}	reciprocal-space vector
$N_{DSP}(\mathbf{r})$	normalised experimental image intensity using DSP method

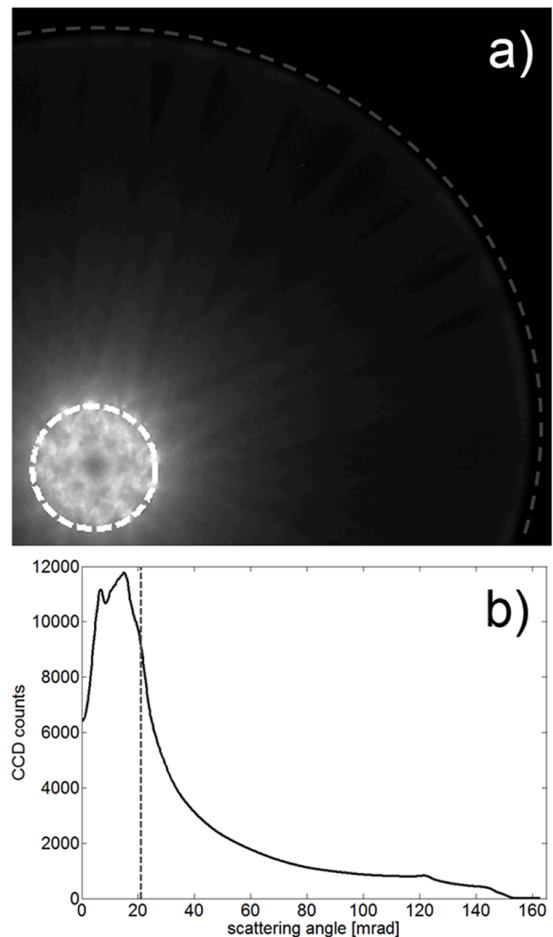


Figure A2. Measurement of outer detector angle. a) Section of Ronchigram on CCD in which the cut-off of signal can be appreciated. White dotted circle represents the BF disk meanwhile grey dotted line shows the cut-off signal. b) Rotationally average from the Ronchigram centre. Dotted line represents the BF disk angle.

$\tilde{N}_{DSP}(\mathbf{r})$	simulated image intensity using a detector sensitivity profile
$\tilde{N}_{HDR}(\mathbf{r})$	simulated image intensity assuming a homogeneous detector response
$\tilde{N}_{HDR}(r_i)$	simulated cross-section value of i th atomic column at position r_i assuming a homogeneous detector response
\mathbf{r}	real-space position vector
r_i	position vector of the i th atomic column
ρ	scattering angle in power-law function
ζ_i	cross-section area of the i th atomic column
σ_{DSP_i}	normalised experimental cross-section of the i th atomic column using DSP method
$\tilde{\sigma}_{DSP_i}$	simulated cross-section of the i th atomic column using detector sensitivity profile
σ_{EFW_i}	normalised experimental cross-section of the i th atomic column using EFW method
$\tilde{\sigma}_{HDR_i}$	simulated cross-section of the i th atomic column assuming a homogeneous detector response
Θ_i	experimental cross-section of the i th atomic column after black-level subtraction
$\xi(\mathbf{r})$	electron flux weighting factor at position \mathbf{r}
$\xi(r_i), \xi_i$	electron flux weighting factor of scattering cross section of i th atomic column at atomic column position r_i
ξ	universal electron flux weighting factor

References

- [1] S. J. Pennycook and D. E. Jesson. High-resolution Z-contrast imaging of crystals. *Ultramicroscopy*, 37:14–38, 1991.
- [2] D. O. Klenov and S. Stemmer. Contributions to the contrast in experimental high-angle annular dark-field images. *Ultramicroscopy*, 106:889–901, 2006.
- [3] D. O. Klenov, S. D. Findlay, L. J. Allen, and S. Stemmer. Influence of orientation on the contrast of high-angle annular dark-field images of silicon. *Physical Review B*, 76:014111, 2007.
- [4] E. J. Kirkland. *Advanced Computing in Electron Microscopy*. Plenum Press, 1998.
- [5] K. Ishizuka. A practical approach for STEM image simulation based on the FFT multislice method. *Ultramicroscopy*, 90:71–83, 2002.
- [6] L. J. Allen, S. D. Findlay, M. P. Oxley, and C. J. Rossouw. Lattice-resolution contrast from a focused coherent electron probe. Part I. *Ultramicroscopy*, 96:47–63, 2003.
- [7] S. D. Findlay, L. J. Allen, M. P. Oxley, and C. J. Rossouw. Lattice-resolution contrast from a focused coherent electron probe. Part II. *Ultramicroscopy*, 96:65–81, 2003.
- [8] M. D. Croitoru, D. Van Dyck, S. Van Aert, S. Bals, and J. Verbeeck. An efficient way of including thermal diffuse scattering in simulation of scanning transmission electron microscopy images. *Ultramicroscopy*, 106:933–940, 2006.
- [9] A. Rosenauer, M. Schowalter, J.T. Titantah, and D. Lamoen. An emission-potential multislice approximation to simulate thermal diffuse scattering in high-resolution transmission electron microscopy. *Ultramicroscopy*, 108:1504–1513, 2008.
- [10] D. A. Muller, B. Edwards, E.J. Kirkland, and J. Silcox. Simulation of thermal diffuse scattering including a detailed phonon dispersion curve. *Ultramicroscopy*, 86:371–380, 2001.
- [11] R. F. Loane, P. Xu, and J. Silcox. Thermal vibrations in convergent-beam electron diffraction. *Acta Crystallographica Section A*, 47(3):267–278, May 1991.
- [12] S. Hillyard and J. Silcox. Detector geometry, thermal diffuse scattering and strain effects in ADF STEM imaging. *Ultramicroscopy*, 58:6–17, 1995.
- [13] K. A. Mkhoyan, S. E. Maccagnano-Zacher, E. J. Kirkland, and J. Silcox. Effects of amorphous layers on ADF-STEM imaging. *Ultramicroscopy*, 108:791–803, 2008.
- [14] S. E. Maccagnano-Zacher, K. A. Mkhoyan, E. J. Kirkland, and J. Silcox. Effects of tilt on high-resolution ADF-STEM imaging. *Ultramicroscopy*, 108:718–726, 2008.
- [15] J. Verbeeck, A. Béch e, and W. Van den Broek. A holographic method to measure the source size broadening in STEM. *Ultramicroscopy*, 120:35–40, 2012.
- [16] V. Grillo. The effect of surface strain relaxation on HAADF imaging. *Ultramicroscopy*, 109:1453–1464, 2009.
- [17] J. M. LeBeau and S. Stemmer. Experimental quantification of annular dark-field images in scanning transmission electron microscopy. *Ultramicroscopy*, 108:1653–1658, 2008.
- [18] A. Rosenauer, K. Gries, K. Mueller, A. Pretorius, M. Schowalter, A. Avramescu, K. Engl, and S. Lutgen. Measurement of specimen thickness and composition in Al_xGa_{1-x}N/GaN using high-angle annular dark field images. *Ultramicroscopy*, 109:1171–1182, 2009.
- [19] J. M. LeBeau, S. D. Findlay, L. J. Allen, and S. Stemmer. Quantitative Atomic Resolution Scanning Transmission Electron Microscopy. *Physical Review Letters*, 100:206101, 2008.
- [20] J. M. LeBeau, S. D. Findlay, X. Wang, A. J. Jacobson, L. J. Allen, and S. Stemmer. High-angle scattering of fast electrons from crystals containing heavy elements: Simulation and experiment. *Physical Review B*, 79:214110, 2009.
- [21] A. Rosenauer, T. Mehrtens, K. Mueller, K. Gries, M. Schowalter, P.V. Satyam, S. Bley, C. Tessarek, D. Hommel, K. Sebald, M. Seyfried, J. Gutowski,

- A. Avramescu, K. Engl, and S. Lutgen. Composition mapping in InGaN by scanning transmission electron microscopy. *Ultramicroscopy*, 111:1316–1327, 2011.
- [22] T. Grieb, K. Mueller, R. Fritz, M. Schowalter, N. Neugebohrn, N. Knaub, K. Volz, and A. Rosenauer. Determination of the chemical composition of GaNAs using STEM HAADF imaging and STEM strain state analysis. *Ultramicroscopy*, 117:15–23, 2012.
- [23] T. Mehrtens, M. Schowalter, D. Tytko, P. Choi, D. Raabe, L. Hoffmann, H. Jönen, U. Rossow, A. Hangleiter, and A. Rosenauer. Measurement of the indium concentration in high indium content InGaN layers by scanning transmission electron microscopy and atom probe tomography. *Applied Physics Letters*, 102(13):132112, 2013.
- [24] V Grillo. An advanced study of the response of ADF detector. *Journal of Physics: Conference Series*, 326(1):012036, 2011.
- [25] K. MacArthur, L. Jones, and P.D. Nellist. How Flat is Your Detector? Non-Uniform Annular Detector Sensitivity in STEM Quantification. *Journal of Physics: Conference Series*, 522:012018, 2014.
- [26] S. D. Findlay and J. M. LeBeau. Detector non-uniformity in scanning transmission electron microscopy. *Ultramicroscopy*, 124:52–60, 2013.
- [27] G. T. Martinez, A. Rosenauer, A. De Backer, J. Verbeeck, and S. Van Aert. Quantitative composition determination at the atomic level using model-based high-angle annular dark field scanning transmission electron microscopy. *Ultramicroscopy*, 137:12–19, 2014.
- [28] S. Van Aert, J. Verbeeck, R. Erni, S. Bals, M. Luysberg, D. Van Dyck, and G. Van Tendeloo. Quantitative atomic resolution mapping using high-angle annular dark field scanning transmission electron microscopy. *Ultramicroscopy*, 109:1236–1244, 2009.
- [29] S. Van Aert, A. De Backer, G. T. Martinez, B. Goris, S. Bals, G. Van Tendeloo, and A. Rosenauer. Procedure to count atoms with trustworthy single-atom sensitivity. *Physical Review B*, 87:064107, 2013.
- [30] H. E. K. E. MacArthur, T. J. Pennycook, E. Okunishi, A. J. D’Alfonso, N. R. Lugg, L. J. Allen, and P. D. Nellist. Probe integrated scattering cross sections in the analysis of atomic resolution HAADF STEM images. *Ultramicroscopy*, 133(0):109 – 119, 2013.
- [31] S. Van Aert, K. J. Batenburg, M. D. Rossel, R. Erni, and G. Van Tendeloo. Three-dimensional atomic imaging of crystalline nanoparticles. *Nature*, 470:374–377, 2011.
- [32] A. De Backer, G. T. Martinez, A. Rosenauer, and S. Van Aert. Atom counting in HAADF STEM using a statistical model-based approach: Methodology, possibilities, and inherent limitations. *Ultramicroscopy*, 134:23–33, 2013.
- [33] G. T. Martinez, A. De Backer, A. Rosenauer, J. Verbeeck, and S. Van Aert. The effect of probe inaccuracies on the quantitative model-based analysis of high angle annular dark field scanning transmission electron microscopy images. *Micron*, pages 57–63, 2013.
- [34] A. De Backer, G.T. Martinez, K.E. MacArthur, L. Jones, A. Béch e, P.D. Nellist, and S. Van Aert. Dose limited reliability of quantitative annular dark field scanning transmission electron microscopy for nano-particle atom-counting. *Ultramicroscopy*, 151(0):56 – 61, 2015. Special Issue: 80th Birthday of Harald Rose; PICO 2015 Third Conference on Frontiers of Aberration Corrected Electron Microscopy.
- [35] A. Rosenauer and M. Schowalter. STEMSIM-a new software tool for simulation of STEM HAADF Z-contrast imaging. *Springer Proceedings in Physics*, 120:169–172, 2007.
- [36] C. Dwyer, C. Maunders, C. L. Zheng, M. Weyland, P. C. Tiemeijer, and J. Etheridge. Sub-0.1nm-resolution quantitative scanning transmission electron microscopy without adjustable parameters. *Applied Physics Letters*, 100(19):191915, 2012.
- [37] A. De Backer, A. De wael, J. Gonnissen, and S. Van Aert. Optimal experimental design for nano-particle atom-counting from high-resolution STEM images. *Ultramicroscopy*, 151(0):46 – 55, 2015. Special Issue: 80th Birthday of Harald Rose; PICO 2015 Third Conference on Frontiers of Aberration Corrected Electron Microscopy.
- [38] James M. LeBeau, Scott D. Findlay, Leslie J. Allen, and Susanne Stemmer. Position averaged convergent beam electron diffraction: Theory and applications. *Ultramicroscopy*, 110(2):118 – 125, 2010.
- [39] Koji Kimoto and Kazuo Ishizuka. Spatially resolved diffractometry with atomic-column resolution. *Ultramicroscopy*, 111(8):1111 – 1116, 2011.
- [40] Z. W. Wang, Z. Y. Li, S. J. Park, A. Abdela, D. Tang, and R. E. Palmer. Quantitative z-contrast imaging in the scanning transmission electron microscope with size-selected clusters. *Phys. Rev. B*, 84:073408, Aug 2011.
- [41] Lewys Jones. Quantitative ADF STEM: acquisition, analysis and interpretation. *Journal of Physics: Conference Series (in review)*, 2015.
- [42] Lewys Jones, Hao Yang, Timothy Pennycook, Matthew Marshall, Sandra Van Aert, Nigel Browning, Martin Castell, and Peter D. Nellist. Smart align A new tool for robust non-rigid registration of scanning microscope data. *Advanced Structural and Chemical Imaging (in press)*, 2015.
- [43] Lewys Jones. Absolute integrator software. 2015. <http://lewjones.com/software/absolute-integrator/>.